


5-2019

Modeling of Complex Parts for Industrial WaterJet Cleaning

Braden James

University of Arkansas, Fayetteville

Follow this and additional works at: <https://scholarworks.uark.edu/etd>

 Part of the [Computer-Aided Engineering and Design Commons](#), [Industrial Engineering Commons](#), [Industrial Technology Commons](#), [Operational Research Commons](#), and the [Robotics Commons](#)

Recommended Citation

James, Braden, "Modeling of Complex Parts for Industrial WaterJet Cleaning" (2019). *Theses and Dissertations*. 3216.
<https://scholarworks.uark.edu/etd/3216>

This Thesis is brought to you for free and open access by ScholarWorks@UARK. It has been accepted for inclusion in Theses and Dissertations by an authorized administrator of ScholarWorks@UARK. For more information, please contact ccmiddle@uark.edu.

Modeling of Complex Parts for Industrial WaterJet Cleaning

A thesis submitted in partial fulfillment of
the requirements for the degree of
Master of Science in Industrial Engineering

by

Braden James
Dartmouth College
Bachelor of Arts in Engineering Sciences, 2015

May 2019
University of Arkansas

This thesis is approved for recommendation to the Graduate Council.

Harry Pierson, Ph.D.
Thesis Chair

Ed Pohl, Ph.D.
Committee Member

Shengfan Zhang, Ph.D.
Committee Member

Abstract

Industrial high-pressure waterjet cleaning is common to many industries. The modeling in this paper functions inside a collaborative robotic framework for high mix, low volume processes where human robot collaboration is beneficial. Automation of pressure washing is desirable for economic and ergonomic reasons. An automated cleaning system needs path simulation and analysis to give the operator insight into the predicted cleaning performance of the system. In this paper, ablation, the removal of a substrate coating by waterjet, is modeled for robotic cleaning operations. The model is designed to work with complex parts often found in spray cleaning operations, namely parts containing hidden portions, holes, or concavities. Experimentation is used to validate and calibrate the ablation model to yield accurate evaluations for how well every feature of a part is cleaned based on the cumulative effect of water affecting the part surface. The ablation model will provide the foundation for optimizing process parameters for robotic waterjet cleaning.

Acknowledgements

I would like to offer special thanks to my patient, supportive advisor Dr. Pierson, the cooperation and generosity of the Red River Army Depot, and the generous support from my family.

Contents

1 Introduction.....	1
2 Literature Review.....	3
3 Methods	6
3.1 Process Modeling.....	6
3.2 Visibility Algorithm.....	10
3.3 Experimentation.....	13
3.3.1 Apparatus	13
3.3.2 Model Parameter Determination.....	15
3.3.3 Validation Experiment.....	18
5 Discussion.....	23
6 Conclusion	29
7 References.....	30
8.1 Appendix A – Experimental Results.....	31
8.2 Appendix B – Validation Data.....	33
8.3 Appendix C – Parameter Estimation Data	35

1 Introduction

Pressure washing is an important industrial process because it offers an effective solution for removing debris and coatings from various materials with little clean up or environmental damage. Automation of pressure washing is desirable for economic reasons such as reduced labor costs and increased machine utilization, as well as worker safety and health concerns [1]. Automated path planning for pressure washing relatively simple parts has been demonstrated [2,3] but remains challenging for complex parts, which for the purposes of this paper are taken to mean parts with some combination of challenging features such as sharp corners, holes, occlusions, overhangs, curvilinear surfaces, concavities, and so forth as exemplified by Figure 1. In practice, tool trajectories for such parts must still be manually programmed on a part-by-part basis. While this might be feasible for long production runs of similar work pieces, pressure washing is often a key process in high-mix, low-volume manufacturing or remanufacturing environments where operations often approach batch-size-of-one. In either case, accurate simulation of robotic pressure washing is needed to evaluate candidate tool paths: It makes manual programming considerably more efficient and is a critical step toward automating the low-volume and one-off operations frequently encountered in remanufacturing. Case in point, this research was inspired by pressure washing operations in a military vehicle depot maintenance facility and is a component of a larger collaborative robotic framework for automating one-off industrial spraying processes.



Figure 1: The figure show an example of a complex part containing holes, pockets, sharp corners, and protrusions. [18]

The practical reality in pressure washing complex parts is that: 1) Non-planar features must be treated; 2) Tool accessibility frequently constrains impingement angle; 3) One generally cannot treat a given workpiece feature without simultaneously affecting adjacent or nearby features having differing shapes and/or orientations; and 4) Features such as protrusions and overhangs shade portions of the workpiece from the spray, and these occlusions vary with tool pose. Consequently, complex parts imply that each feature/surface is likely to receive treatment multiple times from multiple impingement angles with continuously changing offset distances and tool velocities. Existing physical models of pressure washing in the literature assume planar workpieces with the tool axis normal to the surface, constant offset distance, and constant tool velocity. Also implicit is the assumption that the spray cone is never blocked from reaching a given surface by another workpiece feature. These models' output is typically a width or area of coating removed, operating under the assumption that the state of any differential area on the part is binary (cleaned or not cleaned). They do not consider the ablative nature of the process, and therefore cannot be used to model the cumulative effect of multiple passes over the same surface.

This paper proposes a novel physical model for the pressure washing process that maintains the planar workpiece assumption while incorporating impingement angle. The output of the model is a continuous ablation metric, namely the coating thickness removed in a single treatment. Workpieces are modeled as tessellated meshes, and a formal algorithm for computing the accessibility of each planar mesh element, or facet, for a given tool pose is presented. The ablation model is then applied to each facet over the successive treatments throughout the execution of the tool trajectory to predict the cumulative ablation at all points on the workpiece surface.

2 Literature Review

In order to develop a path simulation, a model needs to analyze complex tool trajectories and complex part features. Two notable studies have been conducted to investigate the cleaning properties of high-pressure waterjets. Leu et al. [2] developed an analytical model based on equations defining erosion and crack propagation for a static evaluation of cleaning width, the region where the coating on a substrate is completely removed, on the surface of a planar substrate. Water pressure, nozzle radius, and standoff distance were adjusted. The authors found that the cleaning width increased until a certain optimal standoff distance was reached and then decreased until a critical distance at which no coating was removed. The work piece substrates were flat plates positioned orthogonally to the water jet. Time is not considered in their modeling, implying that the output cleaning width achieves a steady state value slightly smaller than the overall water jet width at some sufficient time over a given area and no additional material removal occurs after that time. In a subsequent study, Leu et al. [3] evaluated a motion trajectory and its effects on cleaning width. Other research utilized an adaptive-network-based fuzzy inference system data analysis tool to map experimental inputs and output values. The

authors did not consider analytical physics-based modeling, asserting the complexity and nonlinear relationships between input parameters and output cleaning results [4]. Guha et al. [5] studied the effects of high speed jet cleaning on orthogonally positioned flat plates and also concluded that material removal decreases nonlinearly with distance. From this research, it is notable that the physics-based models for coating removal are highly complex, even when only considering the analysis of planar substrates. Complex parts introduce greater complexity since the incidence angle at which the water droplets impact the substrate coating must be considered. Additionally, complex parts contain features that will receive ablation indirectly when other features are cleaned. A model for complex parts needs to address this unplanned overlap of cleaning cumulatively such that each pass that affects a given part region increases the ablation depth based on the model parameters.

Research for spray painting and jet cutting address some of the issues concerning complex part simulations. Xia et al. [6] provide an insightful model for depicting paint coverage on a free-form continuous surface using trigonometric relations to predict the rate of surface deposition based on the point distance and angle between the spray source and the target tangential plane. The authors consider angle with respect to the expected thickness of paint deposition over a continuous surface. This research relates trigonometric relationships between the spray source and the surface coating thickness. Chen et al. [7] perform additional work in trajectory optimization for spray painting using a robotic electrostatic rotary bell. Equations are derived to find and optimize the uniformity of the paint deposition. Regions of the part are grouped based on the normal vectors of the facets. Hashish et al. [8] provide insight into modelling of jet cutting and the effects of multiple passes over a given area. The equations and experimentation illustrate a cumulative effect on cutting depth when planned multiple passes are

conducted. The output focus of their modeling is cutting depth rather than width, which will be used in the experiment for this paper. From this research in areas outside of spray cleaning, it can be concluded that more research is needed to evaluate the effects of changing incidence angle and unplanned overlaps in the tool trajectory on ablation depth in spray cleaning. Research on spray painting and jet cutting is limited to parts containing continuous surfaces with gentle curves. Occlusions and cumulative passes will need to be identified in path simulation so that the path planning can be corrected to account for occlusions and unintended increases in coverage. From various positions in a path plan trajectory of a complex part, it is likely that certain areas of a complex part will be hidden by other regions of the part.

Path planning and simulation for highly variable complex geometries provides a multitude of challenges. Most path planning utilizes slicing algorithms that divide the part mesh files. Path plans, in the simplest form, are developed using surface normal values along the slice to determine tool orientation and location [9]. Chen and Zhao [10] utilized more complex free-form surfaces for their analysis of paint deposition. Patches within slices were formed based on the grouping of surfaces that had similar surface normal values. Similar work was done by Sheng et.al [11] for continuous surfaces using bounding boxes around the surface normal values. Kabir et.al [12] developed cleaning algorithms for surface contact tools using robots both to manipulate the part and the cleaning tool, effectively cleaning a rounded surface absent of concavities or other complex features. These processes do not adequately address complex parts featuring holes, concavities, and discontinuous surfaces. In addition, the effects of overlapping passes need to be evaluated when surfaces other than the planned surfaces are subjected to ablation.

Regarding automated path planning for complex parts, Brown & Pierson [13] have proposed a framework for collaborative path planning. The framework includes user interface,

backend, and physical systems. The simulation and the accompanying analysis presented in this paper are essential components of this framework, enabling the user to evaluate the automatically generated tool trajectory and modify the toolpath accordingly.

3 Methods

The model used in the simulation, or visibility algorithm, consists of triangulated meshes in the wavefront (.obj) file format. The model can function with spray cone or part meshes consisting of different sized polygon meshes if needed. These mesh polygons contain facets, which are referred to in this paper as singular triangular components of a mesh bound by defined vertices. The facets will provide the base unit for evaluating parts in the visibility algorithm. The evaluation of the facets will occur iteratively as the tool trajectory is discretized; velocity is converted to time at each tool point. At each tool point, facets that can receive ablation are identified and the ablation levels for each facet are summed over all the discrete points. The algorithm for calculating the facet ablation index is shown in Equation 1,

$$A_i = \sum_{j=0}^F a_{ij} \quad (1)$$

where A is the ablation value assigned to each part facet i and a is the ablation value assigned for every trajectory point j for each facet i , and f is the total trajectory points.

3.1 Process Modeling

The ablation model is formulated to generate a scaled value for each facet of a part mesh based on empirical evaluations of cleanliness. The literature lends insight into the model formulation for the parameters of standoff distance and time. It can be deduced from the literature that time and distance in water jet modeling both function as a power law of the form in Equation 2 [3,5,14].

$$a = K \frac{t^n}{d^m}. \quad (2)$$

Based on empirical evidence from Meng et.al [3], the cleaning width increase to a critical distance and then decreases non-linearly with distance. With respect to velocity, cleaning width appears to decrease nonlinearly with increase velocity. For the purposes of the ablation model and subsequent experimentation, velocity is converted to the duration at discrete positions along the tool trajectory. The trajectory will consist of spray nozzle positions separated by equal time steps.

Three models are considered for evaluation of the effects of time, distance, and angle on ablation depth, defined as the loss of coating depth compared to initial surface levels. Two of the models incorporate the power law while the third considers a generic quadratic surface response function. Due to the uncertainty of how incidence angle will impact levels of ablation, two different treatments for $f(\theta)$ are presented in Equations 3 and 4 (Models 1 and 2). The generic quadratic model (Equation 5, Model 3) is included for comparison to identify the possibility of interactions among the factors.

$$a_i = \frac{K_1 t^n \theta^q}{d^m} \quad (3)$$

$$a_i = K_2 \sin(\theta) \frac{t^n}{d^m} \quad (4)$$

$$a_i = b\theta^2 + ct^2 + ed^2 + f\theta + gt + hd + k\theta t + l\theta d + pdt + r\theta td \quad (5)$$

a is the ablation index assigned to each facet i at each tool trajectory point, t is the time duration assigned to each trajectory point in seconds, θ is the impact angle of the water droplets on the surface in degrees, and d represents the distance between the spray nozzle and the target surface in millimeters. For Equations 3 and 4, K , n , q , and m are empirical constants. Equation 5 (Model 3) contains 10 constants (b , c , e , f , g , h , k , l , p , r) for evaluation. Figure 2 illustrates the distance and angle used in Equations 3-5.

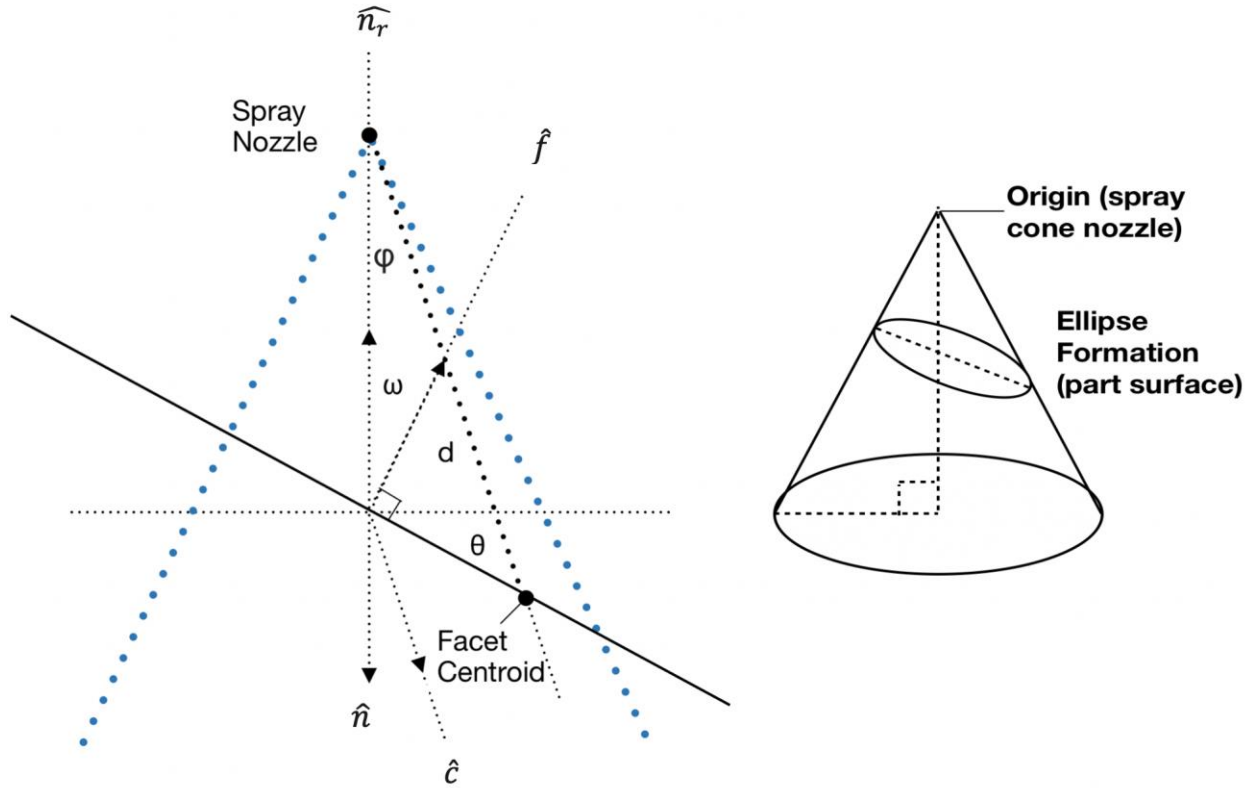


Figure 2: The figure (left) shows how a sample intersection of a part and the spray cone is evaluated, depicting the angle (θ) and distance (d) used for the model calculation. The additional angles and vectors displayed are used for identifying the angle at which water impinges on a facet surface. The figure (right) shows the conic section ellipse formation used to identify the expected width of the thickness reduction region.

In Figure 2, the angle used in the model is calculated trigonometrically using unit vectors positioned at the origin. In Equation 6, φ is defined as the angle between the unit spray cone vector (\hat{n}) and the nozzle to facet centroid unit vector (\hat{c}).

$$\varphi = \arccos\left(\frac{\hat{n} \cdot \hat{c}}{|\hat{n}| |\hat{c}|}\right) \quad (6)$$

Additionally, ω is the angle between the reverse spray cone orientation vector (\hat{n}_r) and the part facet unit normal vector (\hat{f}). Vector (\hat{f}) is always positioned outward away from the interior of the part. The equation for ω is listed as Equation 7.

$$\omega = \arccos\left(\frac{\hat{n}_r \cdot \hat{f}}{|\hat{n}_r| |\hat{f}|}\right) \quad (7)$$

θ is the required model angle in Figure 2 and is defined as the angle at which water impacts the part facet surface. It is found trigonometrically by considering the triangle formed by angles φ , $\omega + 90^\circ$, and θ . The formula is shown in Equation 8. The distance required for the model is calculated using the distance between the trajectory nozzle point (n) and the facet centroid point (s), as shown in Equation 9.

$$\theta = 180^\circ - \varphi - (\omega + 90^\circ) \quad (8)$$

$$d = \sqrt{(s_x - n_x)^2 + (s_y - n_y)^2 + (s_z - n_z)^2} \quad (9)$$

Using these trigonometric relations, experimentation was conducted to yield parameter estimations to fit the model for the particular material and process parameters used. The calibrated model is intended to take preliminary tool trajectory planning and evaluate the cleaning effects as a means of verification prior to the actual cleaning of the part. This model can be easily adapted to fit various industrial water cleaning systems.

The analysis and selection of the models considers the least squares (LS), Akaike Information Criterion (AIC), and Bayesian Information Criterion (BIC) evaluation metrics [15]. The adjusted R^2 metric cannot be utilized for nonlinear models since the assumptions for linear modeling do not apply to nonlinear models. The LS value is generally a good indicator of fit, calculated using residuals. However, it does not consider model complexity. AIC and BIC are common indicators for concluding the truthfulness of models. Both AIC and BIC are penalized likelihood criteria, meaning the values increase with complexity to indicate a less ideal model. The AIC metric possesses a k value that determines the level of penalty for complexity in models. The k value is set to 2, as is consistent with most AIC evaluations [15]. AIC has the potential to prefer a model that is too big while BIC has potential to prefer a model that is too small. They are best used in conjunction. Both values are used as relative measures to compare models, with lower values indicating a model that is closer to the truth [14,15].

3.2 Visibility Algorithm

The development of path analysis requires that the model consider the ablative nature of coating removal via waterjet spraying, the features of complex parts, and the effects of overlapping tool trajectory points. The visibility algorithm is designed to iteratively combine these factors to generate a value indicating the level of ablation for each part facet for the entire trajectory.

The algorithm includes operations that define visible regions of the part and excludes occluded surfaces at each trajectory point. The algorithm first discretizes a trajectory to create a list of points consisting of the spray cone orientations, positions, and times. The conical projection of the waterjet, denoted as volume C in Figures 3 and 4, is then generated as a mesh file based on the parameters of the spray gun and nozzle used in the experimentation. This spray cone mesh modeling can be directly adapted to other spray geometries as well. The algorithm then iterates through the discretized trajectory to identify occlusions and then generate ablation values. For each iterated point, the spray cone mesh, C , is oriented via a rigid body transformation from the original mesh to the specific orientation and location of the trajectory position. The algorithm then determines the facets of the part mesh, denoted P in Figures 3 and 4, that are inside of the cone mesh, C , via the Boolean intersection of C and P , denoted:

$$I = C \cap P \quad (10)$$

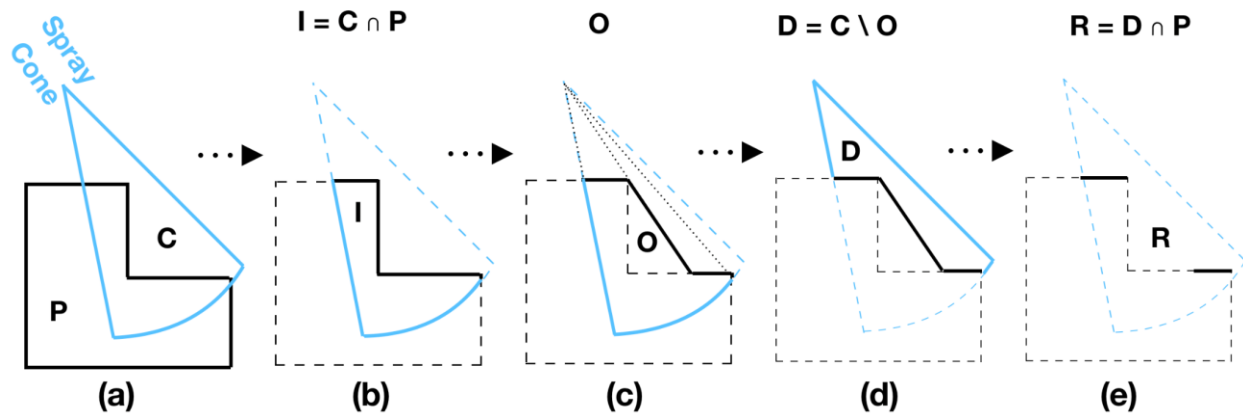


Figure 3: 2-D illustration of Boolean transition from part and cone meshes to only the part facets that can receive ablation from the spray cone at a certain trajectory point. Image (a) shows the union of the spray cone and the part. Image (b) shows the intersection of the part and the spray cone. Image (c) shows the development of the occluded mesh.. Image (d) shows the portion of the cone existing outside of the occluded mesh region. Image (e) shows the remaining regions that can receive ablation.

Mesh volumes are then constructed based on the part facets included in I and the spray cone mesh origin. The volumes extend from the part facets outward away from the spray cone origin. This creates a triangular prism-like mesh volume extending outward from the tool point in order to cast a shadow region. The prism-like polygon meshes that lie inside the spray cone region are all joined together via a Boolean union, yielding a complete shadow region for the specific tool point. The resulting volume union is denoted O . This volume O in Figures 3c encapsulates the space that cannot receive ablation for the given trajectory point. The Boolean difference is then taken between O and the spray cone mesh, C , eliminating the portions of the part mesh that are occluded:

$$D = C \setminus O \quad (11)$$

The facets of the part mesh that are non-occluded and covered by the spray cone mesh, shown as bold black lines in Figure 3e, are then found by the Boolean intersection of the spray cone and the original part mesh:

$$R = D \cap P \quad (12)$$

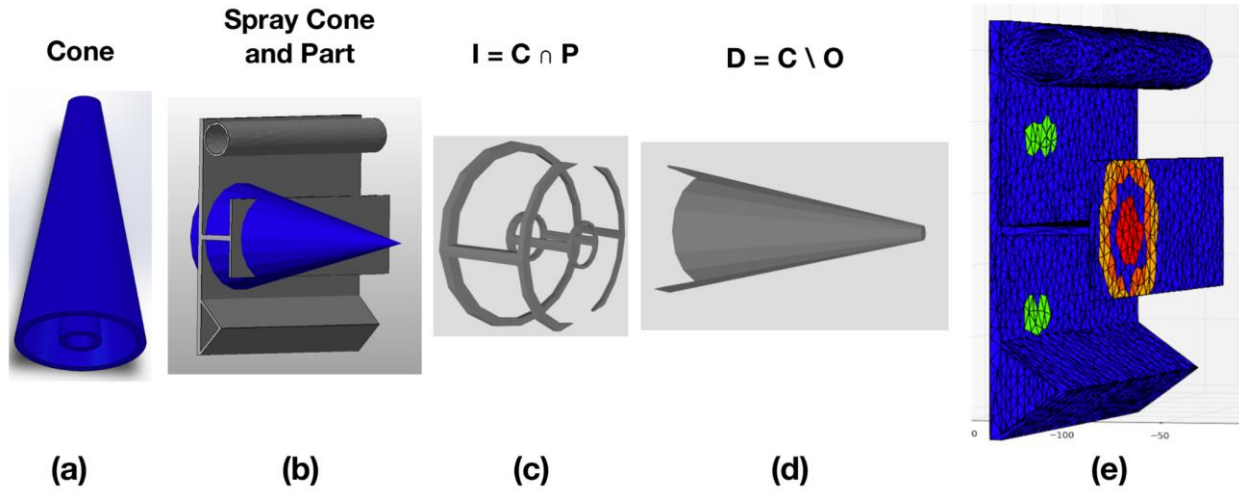


Figure 4: 3-d depiction of the spray cone interacting with a complex part. Note that the spray cone consists of 2 separate cones, consistent with the nozzles used in the experimentation. Image (a) shows the hollow cone geometry. Image (b) shows the mesh union of the part and the cone. Image (c) shows the intersection of the part and the spray cone. Image (d) shows the portion of the cone existing outside of the occluded mesh region. Image (e) shows the final output of the visibility algorithm.

The Boolean transitions are depicted in Figures 3 and 4. The facets of the part mesh found in mesh R are then analyzed for coating thickness reduction based on the parameters: time, distance, and angle. The time component is based on the density of trajectory discretization and is constant for all the facets. However, distance and angle will vary based on the position of the facets. These parameters are found based on the position of each facet centroid and the unit normal vector to the facet surface, as described in Figure 2. The values for the three parameters are then inserted into the aforementioned model, and the ablation value is computed. This process repeats for all the points inside the path plan. The ablation values are summed over all the points. A heat map is generated to show the ablation values. Thresholds may be set defining adequate coverage of the part. This map can be used to identify areas of the part receiving inadequate coverage, allowing the path plan to be optimized.

3.3 Experimentation

The purpose of the experiment was to establish the parameters used in the model in order to generate accurate ablation estimations in the visibility algorithm. This was done on flat plates. Complex test plates were used to validate the model. The experiment aims to determine the parameters of the model and then test the integration of the selected model with the visibility algorithm.

3.3.1 Apparatus

The setup included an apparatus specifically designed for this testing. It can be seen in Figure 5. The apparatus includes several critical components to allow for accurate and consistent testing, including a secure assembly for rotating and changing the distance for the spray gun relative to the workpiece. A movable shutter was added to block the waterjet from reaching the test plates until steady state pressure was reached for the spray system. This shutter was then raised, allowing the waterjet to impact the test surface. The movement of the shutter was monitored by potentiometer connected to a data recorder that recorded angle vs. time. The shutter was also utilized in the validation experiment where complex parts were clamped to the shutter in order to conduct a moving study. The movement of the shutter was monitored by potentiometer connected to a data recorder that recorded angle vs. time. This data was used to accurately measure exposure time on the test plate and to reconstruct the toolpath trajectory of the verification objects.

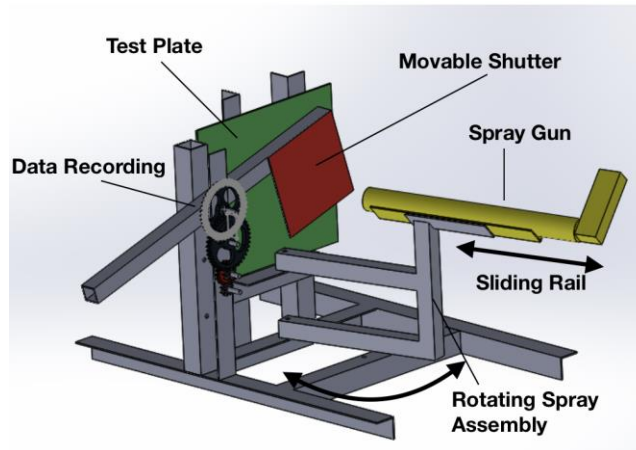


Figure 5: The figure depicts the key features of the spray apparatus allowing it to steadily hold a test plate and adjust the angle and distance of the spray gun.

The spray equipment used was the Aquamiser Ultra BOSS E75V-II with a 40-400 water-only rotary gun. Pressure was set at 30×10^3 psi with flow of 3 gpm. The spray head consists of 4 jets with 3/8-24 jeweled nozzles: 2 jets positioned 12.7 mm ($\frac{1}{2}$ in) from center and 2 jets positioned 7.94 mm ($\frac{5}{16}$ in) from center. The head rotates with a no-load speed of 5200 rpm. The head design and water jet concentric cones can be seen in Figure 6. The spray region utilized in the modeling was defined by two concentric hollow cones representing the area covered by the rotating spray nozzles.

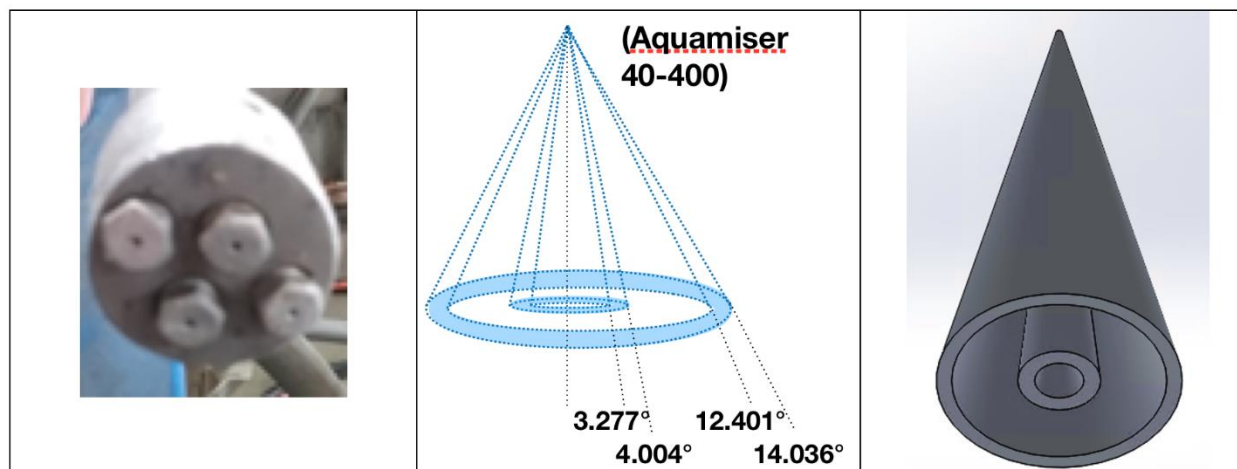


Figure 6: The left image is the Aquamiser 40-400 gun nozzle used in experiment. The middle diagram is the angles defining the angles of water coverage defined by the nozzles. The right image depicts a CAD rendering of the hollow cone to represent the water pressure regions created by the nozzles.

3.3.2 Model Parameter Determination

The test plates used to establish the parameters of the model were 6.35mm (¼ inch) thick mild steel plates measuring 304.8 mm (12 in) square. The plates were sandblasted and hand coated on all sides with military-grade Chemical Agent Resistant Coating (CARC) paint with a coating thickness ranging from 70 to 120 µm. Ablation was measured using a Mitutoyo SJ-210 profilometer. Multiple samples were taken for each test site. One of the test plates used in the experiment is shown in Figure 7. The coating removal region was compared to the unaffected surface.

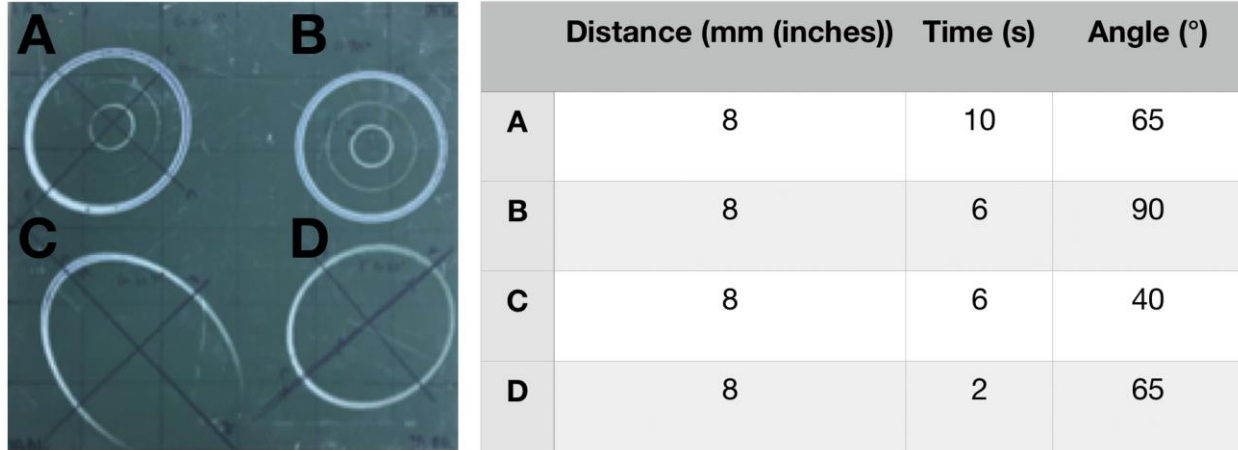


Figure 7: A sample test plate is shown featuring several different test angles and distances, 4 individuals tests on the same plate. Multiple profilometer measurements were taken for each of the tests.

The experiment was conducted using a Box-Benkhin design. The ranges for each factor are listed in Table 1. The design consists of 13 samples as depicted in the Table 2 and Figure 8. The 3 factors were chosen based on initial indications that time, distance, and angle were all significant in affecting surface removal. The factor levels were chosen based on preliminary trials that indicated no measureable ablation beyond $d = 16''$, $\theta = 40^\circ$ (90° being orthogonal to the workpiece), or $t = 10$ s. The maximum distance is consistent with research indicating that the maximum effective spray distance is 150-200 times the nozzle diameter [16]. With a nozzle diameter of $0.08''$, this distance is between 12 and 16 inches. Based on the performance from the first two iterations of the design, it became apparent that a wider range of time would be beneficial. Time was adjusted for the third iteration from a maximum of 10 seconds to 18 seconds. The smaller time factors were also increased.

Table 1: The table shows the 3 values chosen for testing of the 3 experimental factors.

	Low	Med	High
Angle (°)	90	65	40
Distance (mm, (in))	203 (8)	279 (11)	356 (14)
Time (s)	2 (4)	6 (10)	10 (18)

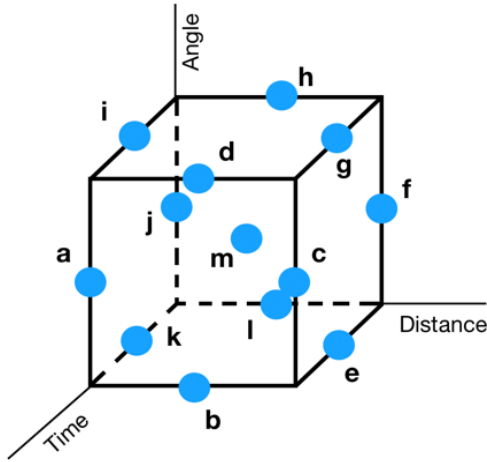


Figure 8: The table shows the Box-Benhkin experimental design combinations for the 3 factors.

Table 2: The table shows the Box-Benhkin experimental design combinations for the 3 factors. The times in parenthesis were used for the third iteration to provide better insight into cleaning behavior.

Box-Benhkin Combinations			
Item	D(mm, (in))	T(s)	$\theta(^{\circ})$
a	203 (8)	10(18)	65
b	279 (11)	10(18)	40
c	356 (14)	10(18)	65
d	279 (11)	10(18)	90
e	356 (14)	6(10)	40
f	356 (14)	2(4)	65
g	356 (14)	6(10)	90
h	279 (11)	2(4)	90
i	203 (8)	6(10)	90
j	203 (8)	2(4)	65
k	203 (8)	6(10)	40
l	279 (11)	2(4)	40
m	279 (11)	6(10)	65

Ablation was measured using a profilometer. The average depth of coating removal was recorded for each test site. A sample of one analyzed profilometer output is shown in Figure 9. A transition region of 1.5 mm was selected for both sides of the thickness reduction region to eliminate areas of abrupt changes in depth between the unaffected regions and the thickness reduction regions of the flat test plates. The thickness reduction region starting point was found by measuring from the probe initial position to the expected beginning of the reduction region on each test plate sample. 2-3 test sites were chosen for each of the 13 samples, each with the same time but different distances and angles relative to the origin of the spray nozzle. Only the test sites that were not cleaned down to bare metal, were considered since the magnitude of this “overtreatment” could not be measured. One of the test plates is shown in Figure 7.

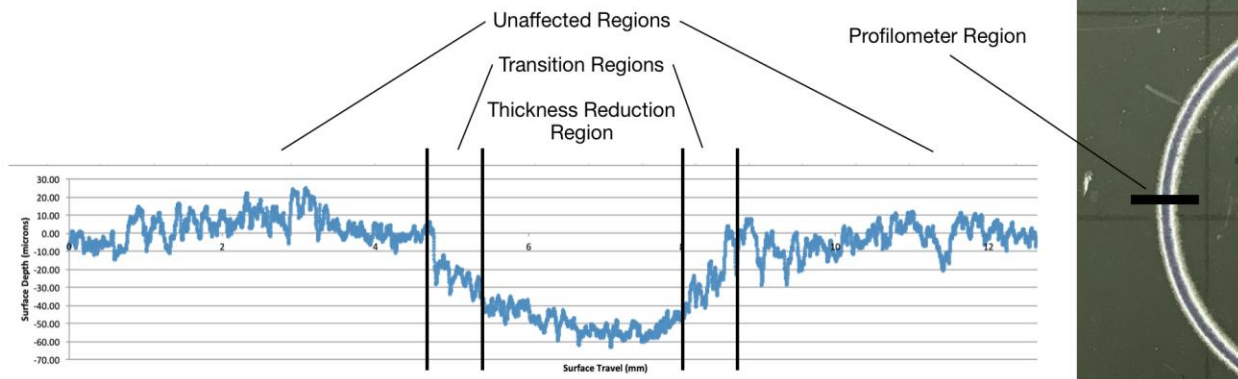


Figure 9: The graph depicts the methodology for identifying the thickness reduction region and eliminating the transition regions from the calculations. The average surface reduction depth was calculated by subtracting the difference of the average unaffected surface from the average of the thickness reduction region. A sample portion of a test plate is shown on the right with a black line marking the area where this profilometer data was acquired.

The distances and angles were evaluated trigonometrically using planes from a conic section defining the spray nozzle, as displayed in Figure 2. The formulation identifies the expected width of the thickness reduction region for different points along the ellipse, or part surface based on relationships of distance and angle. The expected width of the thickness reduction region increases with increased distance and decreased angle. The effects of increased distance and decreased angle are most notable in tests C and D in Figure 7.

The results of the experiment were analyzed using R non-linear least squares parameter estimation in R. This function outputs key metrics, including residuals, fits, least-squares, and AIC/BIC values. The data from this analysis is in Appendix A.

3.3.3 Validation Experiment

The complex parts containing occlusions and discontinuous surfaces were sandblasted and coated similar to the flat test plates. Two unique plates were used as validation surfaces for the model and visibility algorithm. The parts are displayed in Figure 10.

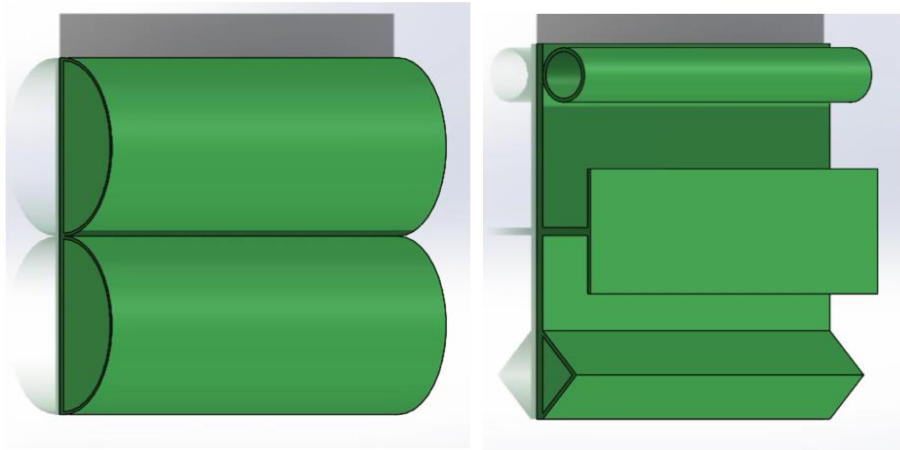


Figure 10: Validation parts featuring Complex Part 1 with curvilinear surfaces (left) and Complex Part 2 with occlusions (right).

The complex parts were sprayed in a motion sequence via clamping to the movable shutter on the test apparatus. With the spray gun held stationary, the plates were impacted by the spray gun in an arc across the parts. Multiple passes were recorded for each of the 4 plates (2 of each complex part in Figure 10) for 8 total motion tests, 2 for each plate. The passes ranged from 1 to 6 passes for each test. The shutter arm trajectory for one of the tests is shown in Figure 11. The time and velocities were recorded using the Arduino and potentiometer, the data for each of which is in Appendix B. The plates were measured using a DeFelsko PosiTector 6000 F1 coating thickness gauge. Thickness data was collected before and after the experimentation on a 50.8mm (2 inches) square grid on each complex part. The mean of 3 measurements from each grid point was used for the before and after measurements. The difference of the means before and after cleaning was recorded as the measured ablation depth for all the grid points. These measurements were then used to compare the visibility algorithm and experiment.

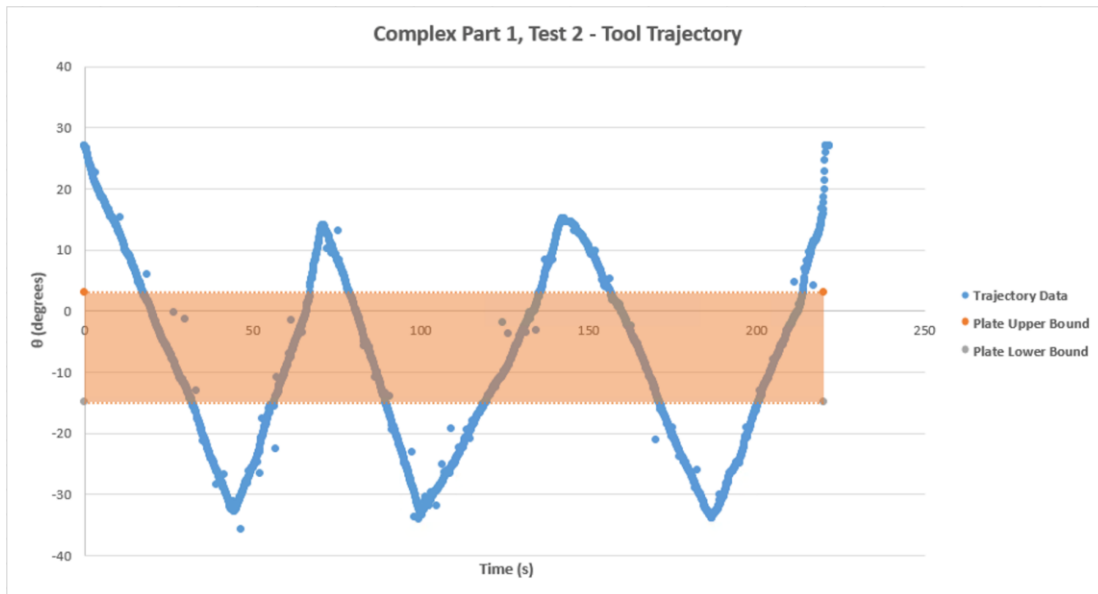


Figure 11: The graph compares time to angle for Complex Part 1: Test 2. The orange band depicts the region where the plate is receiving ablation from the spray gun.

4 Results

The raw data collected from the flat plates (Fig 8) are presented in Appendix A. The parameter estimations and evaluation metrics for each of the evaluated models are shown in Table 3. The p-values for the model parameters are found in Table 4. Model 1 was used in the calculations for the visibility algorithm.

Table 3: The table shows the coefficients of the selected models. Parameter estimates and evaluation metrics are shown.

	Model 1 (Eq 3)	Model 2 (Eq 4)	Model 3 (Eq 5)
Model	$a_i = \frac{K_1 t^n \theta^q}{d^m} (2)$	$a_i = K_2 \sin(\theta) \frac{t^n}{d^m} (6)$	$a_i = b\theta^2 + ct^2 + ed^2 + f\theta + gt + hd + k\theta t + l\theta d + odt + p\theta td (7)$
Parameters	$K_1 = 449.9$	$K_2 = 403.35$	b = -0.01 h = -1.3
	$n = 0.384$	$n = 0.328$	c = 0.14 k = 0.05
	$q = 0.937$		e = -0.087 l = 0.28
	$m = 1.75$	$m = 1.55$	f = 1.02 p = 0.071
			g = -2.88 r = 0.005
LS	7306.1	7342.7	6547.4
AIC (k=2)	455.1	453.4	460.7
BIC	465.4	461.6	483.4

Table 4: The table shows the p-values for each parameter in the 3 models shown.

	P-values	P-value	P-value
Model	$a_i = \frac{K_1 t^n \theta^q}{d^m} (2)$	$a_i = K_2 \sin(\theta) \frac{t^n}{d^m} (6)$	$a_i = b\theta^2 + ct^2 + ed^2 + f\theta + gt + hd + k\theta t + l\theta d + odt + p\theta td (7)$
Parameters	.337	0.311	b: 0.132 h = 0.857
	0.009	0.016	c = 0.661 k = 0.535
	0.021		e = 0.187 l = 0.701
	0.001	0.001	f = 0.113 p = 0.593
			g = 0.476 r = 0.661

Based on these results, the validation experiments shown in Figures 12-14 used Model 1. Figure 12 illustrates the performance of the visibility algorithm in predicting facets that were shaded from the water jet impact. Figures 13 and 14 illustrate the visibility algorithm results and compare these predictions to measurements taken using the coating thickness tester. The 7mm circles taken from the test plates represent the diameter of the thickness tester probe. The probe averages the ablation depth across the diameter.

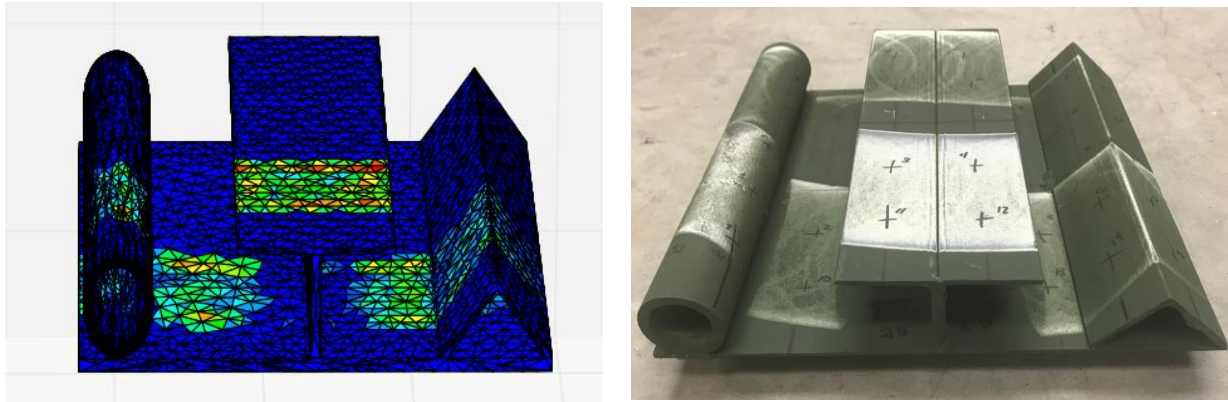


Figure 12: This figure shows the typical results for the ablation and occlusion algorithms for Complex Part 2. The occlusion algorithm can be seen in the central overhang portions of the part that shade the base plate.

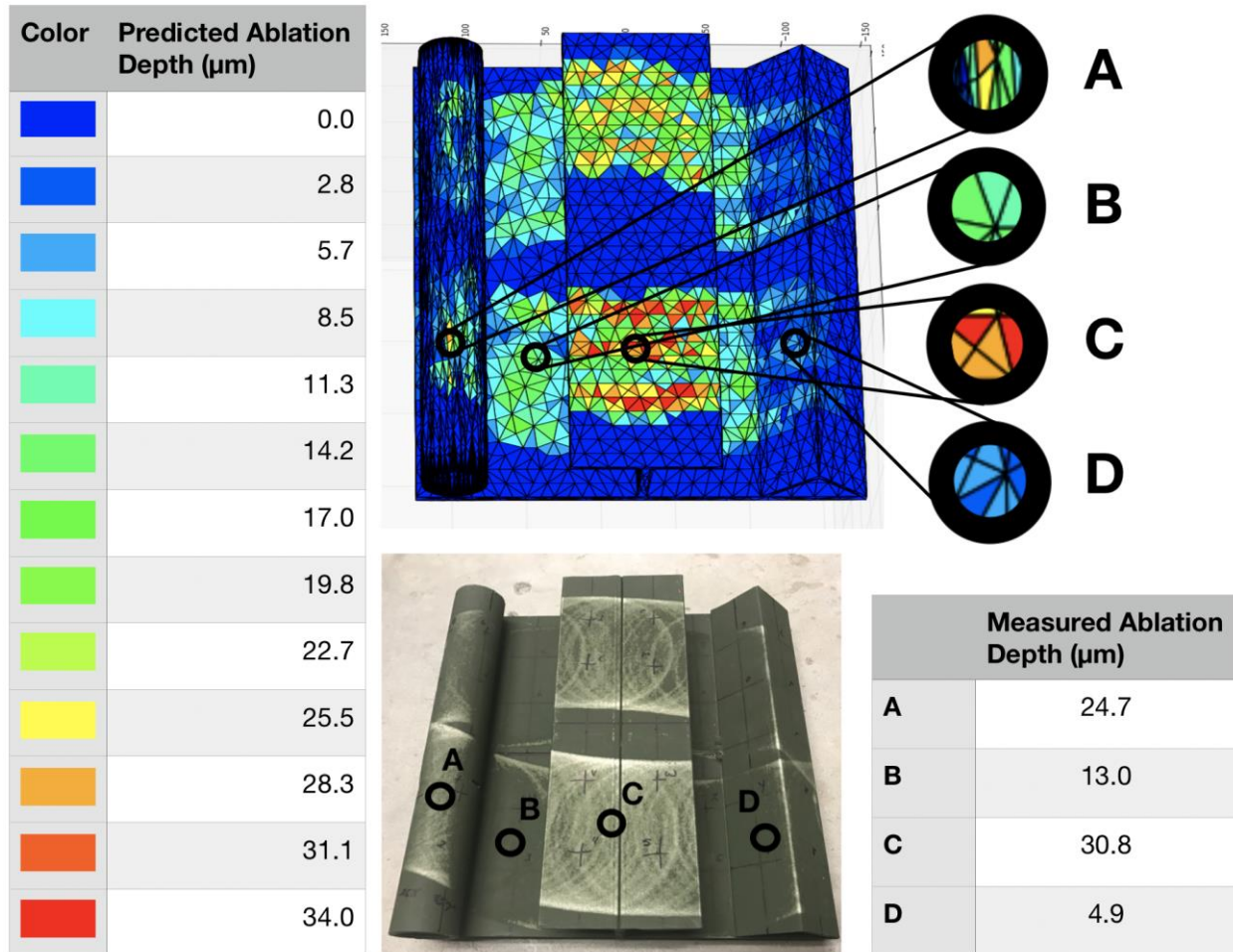


Figure 13: The figure compares the visibility algorithm to the experimental results in the lower right for Complex Part 2. The values for the color schema on the left correspond to the minimum thickness reduction value for the given color.

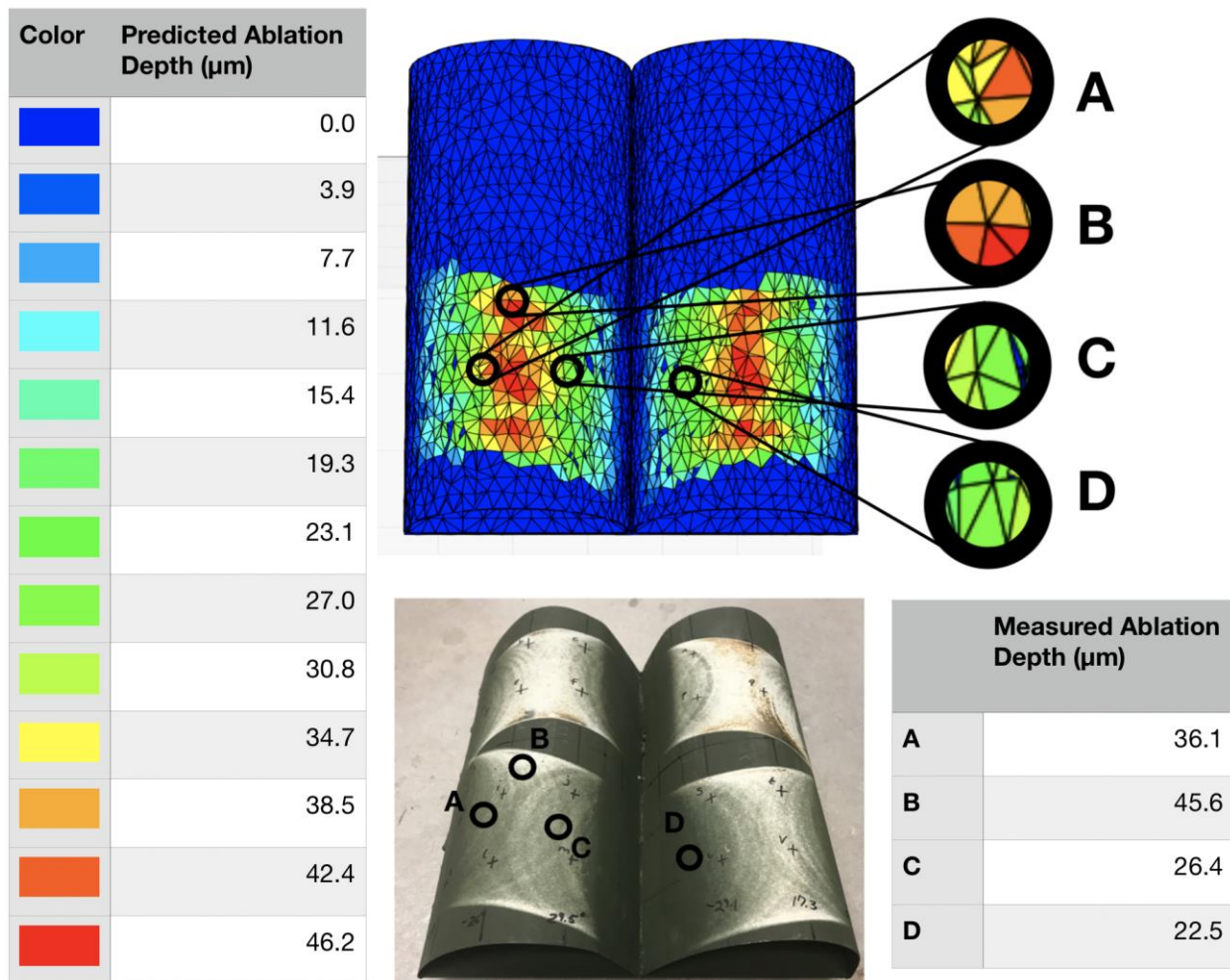


Figure 14: The figure compares the visibility algorithm to the experimental results in the lower right for Complex Part 1. The values for the color schema on the left correspond to the minimum thickness reduction value for the given color.

5 Discussion

Additional models were used for the parameter estimation to verify the use of the proposed model. Table 3 illustrates that Models 1 and 2 are acceptable explanations of the experimental data. The proposed model provides the best solution of the models tested. Models 1 and 2 shown in Table 3 are comparable in terms of accuracy. Model 2 has a slightly improved LS value and slightly worse AIC/BIC values. The quadratic model, Model 3, has a slightly better LS value but is more complex. The better LS value suggests some interaction is occurring in the

model. However, the p-values, located in Table 4, indicate that all interaction terms are insignificant. The additional complexity evident in the higher AIC/BIC values suggest that a quadratic model is likely not the best model. Additionally, the quadratic model possesses no physical meaning. When considering that the quadratic model contains 10 terms and lacks physical meaning, it is likely overfitting the data and absent of physical meaning. It is reasonable to select a simpler model based on these results and the accuracy of the predictions for ablation shown in Figures 13 and 14. For the same reason, additional models featuring more interaction terms were not considered, though more complex models might result in a better fit. When considering nonlinear models, it is best to consider as little terms as possible and only add interaction terms that have a justifiable meaning attached [17]. Given that it is not fully understood how θ interacts with d and t , the simpler models are preferred to explain the data.

Equation 4 (Model 2) does provide an expected formulation for the angular response of the water droplets if the impact was treated as an elastic collision. However, the experimental results are unable to conclude that this treatment is more accurate. A denser sampling of θ is needed to justify altering the use of Model 1 in the visibility algorithm for the ablation response. Additional portions of the experiment could necessitate more in-depth study to characterize θ . Paint adhesion is poorly understood and likely a source of error in the experimentation [4]. Unexpected surface roughness is an additional factor. Regarding the evaluation in this paper, it is unclear whether the incidence angle responds closer to a power model or a trigonometric model.

Since the exponential parameter q in Equation 3 (Model 1) is almost 1, an additional model was considered that assumes a linear relationship for θ , denoted Equation 12. Equation 12 (Model 4) and the analysis are shown in Table 5. The results from the model residuals and fits are in Appendix C. The analysis shows that this simpler model has comparable results to

Equations 3 and 4 (Models 1 and 2). Strong evidence does not exist for which model is the best alternative.

In hindsight, Equation 13 (Model 4) should have been used in the visibility algorithm due to its marginally decreased complexity and comparable accuracy to Equation 3 (Model 1). In Equations 3, 4, and 11, the values for n and m are sensible in respect to previous research evaluating the nonlinear behavior of time and distance in water jet cleaning [3]. Each of the equations include these known physical elements with different treatments for the incidence angle. With n having a value less than 1, this implies a nonlinear increase of ablation at a decreasing rate as time increases. A value greater than 1 for m indicates a decaying level of ablation as distance increases.

Table 5: The table shows the coefficients of Equation 13 considered in the discussion. Parameter estimates and evaluation metrics are shown.

Model	$a_i = K\theta \frac{t^n}{d^m}$ (13)
K	470.1
n	0.393
m	1.78
LS	7309.4
AIC	453.1
BIC	461.4

In Figure 9, the effects of distance and angle are most clearly seen in the horseshoe pattern created in test sites C and D. Trigonometric relations would suggest that the thickness reduction region would increase in size with increased distance and angle. However, other factors are more significant, noted by the opposite characteristics seen in test sites C and D of Figure 9. Pressure decay has likely decreased the cleaning performance [5]. This has caused the

ablative cleaning depth to fade as the distance increases beyond the optimal cleaning distance and the impact angle has decreased across the test site as the distance increased.

For both complex parts utilized in the experiments, a series of moving passes were made over each plate, with average angular velocities calculated over the passes conducted on each plate. The data from the passes can be seen in Appendix B. 4 passes were made over the lower arc depicted in Figure 13 (Complex Part 2, Plate 1) and 6 passes were made over the lower arc depicted in Figure 14 (Complex Part 1, Plate 2). The visibility algorithm results align closely with the actual results for occlusion identification and ablation evaluation. For the second complex part, the occlusion algorithm functions most notable for the center “T” shaped element, where the base plate is shadowed by the angle iron above it. This can be seen in Figures 12 and 13. The first complex part primarily highlights the model’s prediction of ablation for the curved surfaces, showing most notably how changes in the incidence angle affect the ablation depth. Figures 13 and 14 depict a small sample of the total points evaluated in the validation phase. The ablation results shown in Figures 13 and 14 resulted from a multitude of passes over the same part region while the part was attached to the movable shutter on the test apparatus shown in Figure 5. The data from the multiple passes over each validation part was converted to tool trajectories for the visibility algorithm. The nonlinear nature of time in the model was considered in the visibility algorithm. Each tool trajectory point that covered a particular part region was evaluated from the cumulative time that the part region had already been exposed to by previous tool points, if any. This means that as each part region was exposed to more tool points, the time component was evaluated along the curve of the model instead of assuming a starting time of 0 seconds for each tool point.

The geometry of the spray cone is evident in Figures 6, 9, and 13. The inner and outer bands of the spray cone generate streaks of greater ablation depth, shown as a red output from the visibility algorithm. It can be seen particularly well in the Figure 13 that contains large flat regions. This is an expected result; the whiter regions contrasted to the green paint of the experimental image support this, especially along the edges of the cleaning region.

The heat map generated by the visibility algorithm is highly adaptable. The thresholds for maximum and minimum coverage are adjustable as well as the range of colors depicted in-between. The adjustable thresholds can allow for quick modifications to the path planning for reiterations as needed. For the complex parts, the heat map did show some inconsistencies, likely due to coarse mesh density. While this improves computation time, it does introduce the potential for facets of the part to be skipped by the algorithm. The occlusion algorithm is also conservative in that all facets that have a potential to partially occlude another facet of the part mesh are included in the occlusion evaluation. The visibility algorithm did provide a thorough analysis of these complex parts, providing a significant insight into robotic water cleaning analysis.

This visibility algorithm effectively yields an output that can be utilized inside the collaborative framework of a high-mix, low volume industrial process. Figure 15 depicts the collaborative framework where this research would be utilized in both path simulation and path analysis modules. This research covers user interface and backend module components. The algorithms for occlusion identification and ablation estimation provide the analysis component. The heat map generated from the algorithm provides the user interface component so the operator can visually see how cleaning is quantified and the level of cleaning to expect from the given path plan.

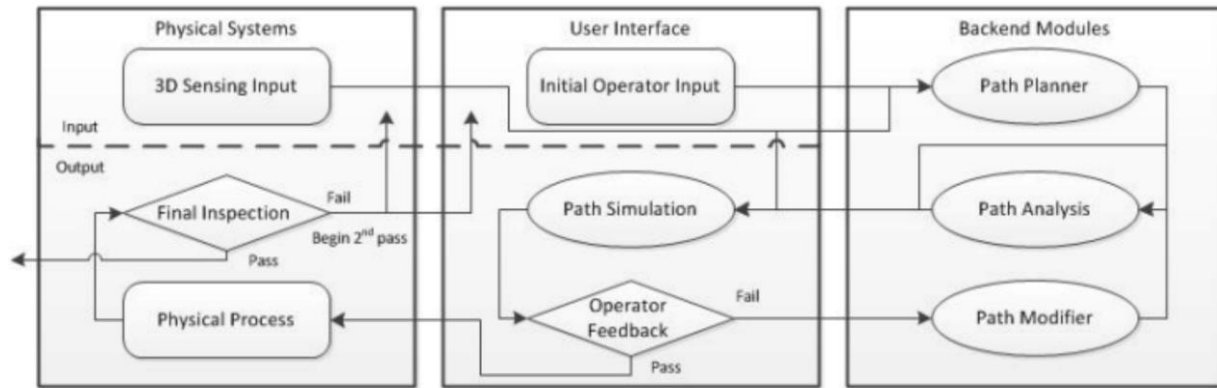


Figure 15: The figure illustrates the collaborative framework for a high-mix, low volume industrial process. The spray cleaning research in this paper would include both path simulation and path analysis modules [13].

The model and methodology proposed in this paper are useful for other applications within spray cleaning and other areas. The model parameters estimated in this research are only suitable for the parameters and materials in the experimentation, including the specific test material, coating and Aquamiser cleaning system. The model and methodology can be expanded to other waterjet cleaning applications with different parameter estimations with additional experimental analysis using new materials and cleaning systems.

The methodology in this paper is likely useful in other applications beyond water cleaning. Different models could be developed using the same methodology to address media blasting and metal Additive Manufacturing (AM). Media applications include spray painting, shot peening, sand and soda blasting, BattleJacket is an example application utilized in the military where sealant is sprayed onto surfaces such as fuel tanks. Minimum and maximum coverage must be considered, which is done inside the proposed algorithm. Shot peening in AM could utilize the methodology of our model, especially given that one-off shot peening is conducted on complex parts.

6 Conclusion

A model has been created to show the path simulation and analysis of a robotic spray cleaning trajectory prior to cleaning for high mix, low volume complex parts. Levels of ablation and occlusion have been shown in a simulated environment that gives the operator insight into path analysis for robotic cleaning. The model is able to identify hidden portions, holes, and concavities and exclude portions of the part that are likely occluded at various points along a spray trajectory. The model shows the cumulative effects of ablation for multiple passes that overlap or indirectly cover various part facets. Experimentation calibrated the visibility algorithm and validated the path simulation model using complex parts. The model and methodology can be applied to other water cleaning systems and other applications.

7 References

- [1] A. Woods and H. A. Pierson, "Developing an Ergonomic Model and Automation Justification for Spraying Operations," *Inst. Ind. Syst. Eng. Annu. Conf.*, 2018.
- [2] M. C. Leu, P. Meng, E. S. Geskin, and L. Tismeneskiy, "Mathematical Modeling and Experimental Verification of Stationary Waterjet Cleaning Process," *J. Manuf. Sci. Eng.*, vol. 120, no. August, p. 571, 1998.
- [3] P. Meng, E. S. Geskin, M. C. Leu, F. Li, and L. Tismeneskiy, "an Analytical and Experimental Study of Cleaning with Moving Waterjets," vol. 120, no. August 1998, pp. 580–589, 1998.
- [4] G. Daoming and C. Jie, "ANFIS for high-pressure waterjet cleaning prediction," *Surf. Coatings Technol.*, vol. 201, no. 3–4, pp. 1629–1634, Oct. 2006.
- [5] A. Guha, R. M. Barron, and R. Balachandar, "An experimental and numerical study of water jet cleaning process," *J. Mater. Process. Technol.*, vol. 211, no. 4, 2011.
- [6] W. Xia, S. Yu, and X. Liao, "Paint deposition pattern modeling and estimation for robotic air spray painting on free-form surface using the curvature circle method," *Ind. Robot An Int. J.*, vol. 37, no. 2, pp. 202–213, 2010.
- [7] W. Chen, H. Liu, Y. Tang, and J. Liu, "Trajectory Optimization of Electrostatic Spray Painting Robots on Curved Surface," *Coatings*, vol. 7, no. 10, p. 155, 2017.
- [8] M. Hashish and M. P. DuPlessis, "Prediction Equations Relating High Velocity Jet Cutting Performance to Stand Off Distance and Multipasses," vol. 101, pp. 311–318, 1979.
- [9] Z. He, B. Lu, J. Hong, Y. Wang, and Y. Tang, "A novel arc-spraying robot for rapid tooling," *Int. J. Adv. Manuf. Technol.*, vol. 31, no. 9–10, pp. 1012–1020, 2007.
- [10] W. Chen and D. Zhao, "Path Planning for Spray Painting Robot of Workpiece Surfaces," *Math. Probl. Eng.*, vol. 2013, pp. 1–6, 2013.
- [11] W. Sheng, N. Xi, M. Song, Y. Chen, and P. MacNeille, "Automated CAD-guided robot path planning for spray painting of compound surfaces," *IEEE Int. Conf. Intell. Robot. Syst.*, vol. 3, pp. 1918–1923, 2000.
- [12] A. M. Kabir *et al.*, "Planning algorithms for multi-setup multi-pass robotic cleaning with oscillatory moving tools," *IEEE Int. Conf. Autom. Sci. Eng.*, vol. 2016–Novem, pp. 751–757, 2016.
- [13] S. Brown and H. A. Pierson, "A Collaborative Framework for Robotic Task Specification," *Procedia Manuf.*, vol. 17, pp. 270–277, 2018.
- [14] D. A. Summers, *WaterJetting Technology*, 1st ed. E & FN Spon, 1995.
- [15] K. P. Burnham and D. R. Anderson, "Multimodel Inference," *Sociol. Methods Res.*, vol. 33, no. 2, pp. 261–304, 2004.
- [16] G. Casella and R. L. Berger, "Statistical inference (2nd ed.)," vol. 1, no. September. p. 660, 2002.
- [17] P. Karaca-Mandic, E. C. Norton, and B. Dowd, "Interaction terms in nonlinear models," *Health Serv. Res.*, vol. 47, no. 1 PART 1, pp. 255–274, 2012.
- [18] Wapcaplet, "Engine Block - Top," 2004. .

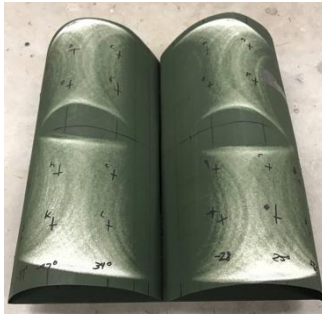
8.1 Appendix A – Experimental Results

The results from the experiment to establish the model parameters are below. A total of 58 data points were collected from the test plates. The nominal test values are shown below. The actual measurements are calculated trigonometrically based on the location of the test site on the test plate sample.

Test_ID	Measured Ablation Depth (μm)	Distance (in)	Time (s)	Theta (°)	Actual Distance (in)	Actual Time (s)	Actual Angle (°)
1ABL_M	10.84	8	6	40	8.2	5.10	39.00
1ABR_C	36.50	8	2	65	7.4	1.98	77.00
1ABR_F	13.01	8	2	65	9.1	1.98	53.00
1ABR_M	29.95	8	2	65	8.2	1.98	63.38
1ATL_F	33.75	8	10	65	9.1	11.39	53.00
1ATL_M	46.19	8	10	65	8.2	11.39	63.38
1BBR_C	41.60	11	10	40	9.0	9.04	52.00
1BBR_M	15.27	11	10	40	11.2	9.04	39.00
1BTL	11.35	11	10	90	11.2	9.63	87.75
1BTR_C	20.92	11	2	40	9.0	1.64	52.00
2ABL_C	19.29	8	6	40	6.5	6.01	52.00
2ATL_C	59.87	14	10	65	13.0	10.03	77.00
2ATL_F	3.46	14	10	65	15.9	10.03	53.00
2ATL_M	8.67	14	10	65	14.3	10.03	63.38
2BBL_C	13.92	11	6	40	9.0	6.15	52.00
2BTL	3.98	14	6	90	14.3	5.96	87.75
2BTR_C	12.23	14	10	65	13.0	10.29	77.00
2BTR_M	4.98	14	10	65	14.3	10.29	63.38
3ABL_F	16.02	8	10	65	9.1	9.73	53.00
3ABL_M	25.98	8	10	65	8.2	9.73	63.38
3ATL	2.05	14	2	65	14.3	1.82	63.38
3ATR	4.80	14	6	90	14.3	5.92	87.75
3BBL_C	38.67	11	10	40	9.0	9.89	52.00
3BBL_M	7.54	11	10	40	11.2	9.89	39.00
3BTL_C	4.02	8	2	65	7.4	2.11	77.00
3BTL_F	-3.81	8	2	65	9.1	2.11	53.00
3BTL_M	17.08	8	2	65	8.2	2.11	63.38
3BTR_M	8.08	8	6	40	8.2	5.74	39.00
4ABR_C	21.32	11	2	40	9.0	2.50	52.00
4ABR_M	4.40	11	2	40	11.2	2.50	39.00
4ATL_1	27.00	11	10	90	11.2	9.92	87.75

Test_ID	Measured Ablation Depth (μm)	Distance (in)	Time (s)	Theta (°)	Actual Distance (in)	Actual Time (s)	Actual Angle (°)
4ATL_2	38.36	11	10	90	11.2	9.92	87.75
4ATR_1	7.74	11	2	90	11.2	1.87	87.75
4ATR_2	25.06	11	2	90	11.2	1.87	87.75
4BBL_C	20.13	8	4	65	7.4	4.20	77.00
4BBL_F	7.78	8	4	65	9.1	4.20	53.00
4BBL_M	19.40	8	4	65	8.2	4.20	63.38
4BTL_C	17.79	11	6	65	10.2	5.90	77.00
4BTL_F	-0.10	11	6	65	12.5	5.90	53.00
4BTL_M	10.45	11	6	65	11.2	5.90	63.38
4BTR_F	19.96	8	18	65	9.1	17.76	53.00
4BTR_M	27.58	8	18	65	9.1	17.76	53.00
5ABR_M	11.14	10	18	40	10.2	18.27	39.00
5ATL_M	3.79	8	10	40	8.2	10.16	39.00
5BBL_F	12.58	10	10	65	11.3	10.14	53.00
5BBL_M	14.25	10	10	65	10.2	10.14	63.38
5BTL_1	15.42	10	4	90	10.2	4.18	87.75
5BTL_2	17.21	10	4	90	10.2	4.18	87.75
5BTR_C	47.49	10	4	40	8.2	4.17	52.00
5BTR_M	12.16	10	4	40	10.2	4.17	39.00
6ABL_C	9.61	12	4	65	11.2	4.22	77.00
6ABL_M	11.39	12	4	65	12.3	4.22	63.38
6ATL_C	16.57	12	18	65	11.2	17.80	77.00
6ATL_F	0.61	12	18	65	13.6	17.80	53.00
6ATL_M	26.24	12	18	65	12.3	17.80	63.38
6ATR_C	23.35	12	10	40	9.8	10.18	52.00
6ATR_M	5.49	12	10	40	12.3	10.18	39.00
6BTL_1	9.51	12	10	90	12.3	10.12	87.75

8.2 Appendix B – Validation Data



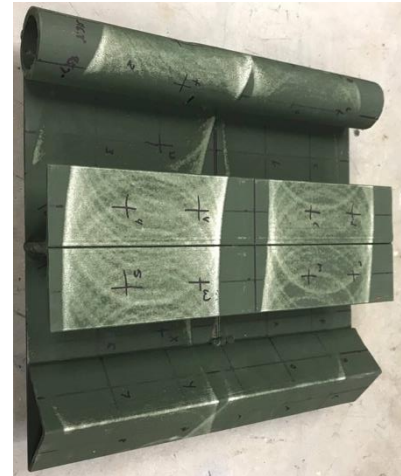
The complex parts were spray cleaned using the apparatus described in the experiment, yielding an angular velocity for each pass. This data is presented here. For Complex Part 1, Plate 1 is shown on the left and plate 2 on the right. The left side corresponds to the lower arc in both images and the right side corresponds to the upper arcs.



Complex Part 1					
Set	FILE_ID	Total Time (s)	Total Degrees (°)	Average Ang Vel (°/s)	Total Passes
Plate 1	8", 90°				
Left					2
4	bmj1	14.91	66.46	4.46	
	bmj2	42.69	63.15	1.48	
Right	8", 90°				1
4	bmj4	64.87	59.32	0.91	
Plate 2					
Left	8", 65°				2
4	bmj5	53.57	60.90	1.14	
	bmj6	48.35	64.61	1.34	
Right	8", 90°				6
5	bmj7	44.48	59.71	1.34	
		19.50	29.66	1.52	
	bmj8	7.04	17.08	2.43	
		30.66	45.94	1.50	
		39.85	47.00	1.18	
		44.29	48.86	1.10	
33.94	60.77	1.79			



For Complex Part 2, Plate 1 is shown on the left and plate 2 on the right. The left and right sides correspond to the left and right in the perspectives of the images shown.



Complex Part 2					
Set	FILE_ID	Total Time	Tot Degrees (°)	Average Ang Vel (°/s)	Total Passes
Plate 1					
Left	6.5", 90°				2
5	0	67.92	63.82	0.94	
	1	71.61	63.68	0.89	
Right	8", 90°				3
5	2	62.42	59.98	0.96	
		43.54	51.50	1.18	
		45.88	51.90	1.13	
Plate 2					
Left	6.5",90°				4
	3	53.70	61.57	1.15	
		40.07	50.44	1.26	
		38.71	51.64	1.33	
		38.59	62.89	1.63	
Right	6.5",65°				3
	4	47.14	60.51	1.28	
		41.04	50.05	1.22	
		43.02	52.83	1.23	

8.3 Appendix C – Parameter Estimation Data

The data includes fits vs residuals for all the models tested.

Surface Micrometer Measure Depth (μm)	Actual Time (s)	Actual Angle ($^{\circ}$)	Actual Distance (in)	Eq 3 (Model 1)		Eq 4 (Model 2)	
				Residuals	Fits	Residuals	Fits
10.845	5.102	39.000	8.176	-3.433	14.278	-5.662	16.507
36.499	1.977	77.000	7.441	16.764	19.735	14.815	21.684
13.009	1.977	53.000	9.079	-1.448	14.456	-0.036	13.045
29.949	1.977	63.375	8.176	10.800	19.149	12.765	17.184
33.750	11.390	53.000	9.079	8.202	25.548	10.588	23.162
46.185	11.390	63.375	8.176	13.308	32.877	15.675	30.511
41.597	9.039	52.000	8.973	17.613	23.983	20.022	21.575
15.273	9.039	39.000	11.242	7.250	8.024	3.138	12.135
11.352	9.630	87.750	11.242	-11.976	23.328	-8.320	19.672
20.918	1.638	52.000	8.973	7.229	13.689	8.594	12.324
19.293	6.010	52.000	6.526	-7.571	26.864	-11.657	30.950
59.866	10.030	77.000	13.022	41.795	18.072	44.398	15.469
3.456	10.030	53.000	15.887	4.188	-0.732	-5.850	9.306
8.669	10.030	63.375	14.308	-1.951	10.619	-3.590	12.259
13.924	6.150	52.000	8.973	-6.985	20.909	-4.939	18.863
3.975	5.961	87.750	14.308	-4.774	8.749	-7.578	11.553
12.225	10.288	77.000	13.022	-5.987	18.212	-3.373	15.598
4.982	10.288	63.375	14.308	-5.757	10.739	-7.379	12.361
16.018	9.732	53.000	9.079	-8.695	24.712	-5.980	21.998
25.977	9.732	63.375	8.176	-5.600	31.577	-3.000	28.977
2.046	1.823	63.375	14.308	1.264	0.782	-4.963	7.009
4.796	5.922	87.750	14.308	-3.912	8.709	-6.732	11.529
38.668	9.887	52.000	8.973	14.114	24.555	16.450	22.219
7.537	9.887	39.000	11.242	-0.946	8.484	-4.960	12.497
4.023	2.106	77.000	7.441	-16.063	20.086	-18.115	22.138
-3.808	2.106	53.000	9.079	-18.521	14.713	-17.126	13.318
17.075	2.106	63.375	8.176	-2.366	19.442	-0.469	17.544
8.083	5.739	39.000	8.176	-6.854	14.938	-9.073	17.156
21.320	2.502	52.000	8.973	5.938	15.382	7.160	14.160
4.396	2.502	39.000	11.242	4.116	0.280	-3.569	7.965
27.003	9.922	87.750	11.242	3.393	23.609	7.137	19.866
38.360	9.922	87.750	11.242	14.750	23.609	18.494	19.866
7.742	1.874	87.750	11.242	-2.698	10.440	-3.761	11.503

Surface Micrometer Measure Depth (μm)	Actual Time (s)	Actual Angle ($^{\circ}$)	Actual Distance (in)	Eq 3 (Model 1)		Eq 4 (Model 2)	
				Residuals	Fits	Residuals	Fits
25.062	1.874	87.750	11.242	14.621	10.440	13.559	11.503
20.129	4.195	77.000	7.441	-5.248	25.377	-7.619	27.749
7.785	4.195	53.000	9.079	-10.673	18.457	-8.909	16.694
19.402	4.195	63.375	8.176	-4.370	23.771	-2.589	21.991
17.789	5.898	77.000	10.232	-4.978	22.767	-1.121	18.911
-0.096	5.898	53.000	12.483	-9.950	9.854	-11.473	11.377
10.453	5.898	63.375	11.242	-7.790	18.243	-4.533	14.987
19.964	17.763	53.000	9.079	-4.347	24.310	-6.831	26.794
27.583	17.763	53.000	9.079	3.273	24.310	0.789	26.794
11.137	18.269	39.000	10.220	2.119	9.019	-6.588	17.725
3.792	10.156	39.000	8.176	-13.781	17.573	-16.894	20.686
12.579	10.141	53.000	11.348	-5.273	17.851	-3.181	15.760
14.249	10.141	63.375	10.220	-11.766	26.015	-6.511	20.760
15.419	4.181	87.750	10.220	-2.273	17.691	-1.936	17.355
17.214	4.181	87.750	10.220	-0.477	17.691	-0.141	17.355
47.490	4.174	52.000	8.157	27.034	20.456	28.068	19.422
12.164	4.174	39.000	10.220	5.498	6.666	1.239	10.924
9.606	4.223	77.000	11.162	-7.732	17.337	-5.198	14.804
11.395	4.223	63.375	12.264	-0.956	12.351	-0.337	11.732
16.572	17.803	77.000	11.162	-9.638	26.210	-7.155	23.727
0.609	17.803	53.000	13.618	-7.750	8.360	-13.665	14.274
26.236	17.803	63.375	12.264	7.847	18.390	7.433	18.803
23.349	10.179	52.000	9.789	0.989	22.360	3.756	19.593
5.487	10.179	39.000	12.264	0.444	5.043	-5.533	11.020
9.507	10.121	87.750	12.264	-10.481	19.988	-7.959	17.465

Surface Micrometer Measure Depth (μm)	Actual Time (s)	Actual Angle ($^{\circ}$)	Actual Distance (in)	Eq 5 (Model 3)		Eq 13 (Model 4)	
				Residuals	Fits	Residuals	Fits
10.845	5.102	39.000	8.176	-3.433	14.278	-5.662	16.507
36.499	1.977	77.000	7.441	16.764	19.735	14.815	21.684
13.009	1.977	53.000	9.079	-1.448	14.456	-0.036	13.045
29.949	1.977	63.375	8.176	10.800	19.149	12.765	17.184
33.750	11.390	53.000	9.079	8.202	25.548	10.588	23.162
46.185	11.390	63.375	8.176	13.308	32.877	15.675	30.511
41.597	9.039	52.000	8.973	17.613	23.983	20.022	21.575
15.273	9.039	39.000	11.242	7.250	8.024	3.138	12.135
11.352	9.630	87.750	11.242	-11.976	23.328	-8.320	19.672
20.918	1.638	52.000	8.973	7.229	13.689	8.594	12.324
19.293	6.000	52.000	6.526	-7.571	26.864	-11.657	30.950
59.866	10.030	77.000	13.022	41.795	18.072	44.398	15.469
3.456	10.030	53.000	15.887	4.188	-0.732	-5.850	9.306
8.669	10.030	63.375	14.308	-1.951	10.619	-3.590	12.259
13.924	6.000	52.000	8.973	-6.985	20.909	-4.939	18.863
3.975	5.961	87.750	14.308	-4.774	8.749	-7.578	11.553
12.225	10.288	77.000	13.022	-5.987	18.212	-3.373	15.598
4.982	10.288	63.375	14.308	-5.757	10.739	-7.379	12.361
16.018	9.732	53.000	9.079	-8.695	24.712	-5.980	21.998
25.977	9.732	63.375	8.176	-5.600	31.577	-3.000	28.977
2.046	1.823	63.375	14.308	1.264	0.782	-4.963	7.009
4.796	5.922	87.750	14.308	-3.912	8.709	-6.732	11.529
38.668	9.887	52.000	8.973	14.114	24.555	16.450	22.219
7.537	9.887	39.000	11.242	-0.946	8.484	-4.960	12.497
4.023	2.106	77.000	7.441	-16.063	20.086	-18.115	22.138
-3.808	2.106	53.000	9.079	-18.521	14.713	-17.126	13.318
17.075	2.106	63.375	8.176	-2.366	19.442	-0.469	17.544
8.083	5.739	39.000	8.176	-6.854	14.938	-9.073	17.156
21.320	2.502	52.000	8.973	5.938	15.382	7.160	14.160
4.396	2.502	39.000	11.242	4.116	0.280	-3.569	7.965
27.003	9.922	87.750	11.242	3.393	23.609	7.137	19.866
38.360	9.922	87.750	11.242	14.750	23.609	18.494	19.866
7.742	1.874	87.750	11.242	-2.698	10.440	-3.761	11.503
25.062	1.874	87.750	11.242	14.621	10.440	13.559	11.503
20.129	4.195	77.000	7.441	-5.248	25.377	-7.619	27.749
7.785	4.195	53.000	9.079	-10.673	18.457	-8.909	16.694
19.402	4.195	63.375	8.176	-4.370	23.771	-2.589	21.991

Surface Micrometer Measure Depth (μm)	Actual Time (s)	Actual Angle ($^{\circ}$)	Actual Distance (in)	Eq 5 (Model 3)		Eq 13 (Model 4)	
				Residuals	Fits	Residuals	Fits
17.789	5.898	77.000	10.232	-4.978	22.767	-1.121	18.911
-0.096	5.898	53.000	12.483	-9.950	9.854	-11.473	11.377
10.453	5.898	63.375	11.242	-7.790	18.243	-4.533	14.987
19.964	17.763	53.000	9.079	-4.347	24.310	-6.831	26.794
27.583	17.763	53.000	9.079	3.273	24.310	0.789	26.794
11.137	18.269	39.000	10.220	2.119	9.019	-6.588	17.725
3.792	10.156	39.000	8.176	-13.781	17.573	-16.894	20.686
12.579	10.141	53.000	11.348	-5.273	17.851	-3.181	15.760
14.249	10.141	63.375	10.220	-11.766	26.015	-6.511	20.760
15.419	4.181	87.750	10.220	-2.273	17.691	-1.936	17.355
17.214	4.181	87.750	10.220	-0.477	17.691	-0.141	17.355
47.490	4.174	52.000	8.157	27.034	20.456	28.068	19.422
12.164	4.174	39.000	10.220	5.498	6.666	1.239	10.924
9.606	4.223	77.000	11.162	-7.732	17.337	-5.198	14.804
11.395	4.223	63.375	12.264	-0.956	12.351	-0.337	11.732
16.572	17.803	77.000	11.162	-9.638	26.210	-7.155	23.727
0.609	17.803	53.000	13.618	-7.750	8.360	-13.665	14.274
26.236	17.803	63.375	12.264	7.847	18.390	7.433	18.803
23.349	10.179	52.000	9.789	0.989	22.360	3.756	19.593
5.487	10.179	39.000	12.264	0.444	5.043	-5.533	11.020
9.507	10.121	87.750	12.264	-10.481	19.988	-7.959	17.465